ICAS 2021 SHANG HAI
International Council of the Aeronautical Sciences
32nd Congress of the International Council of the Aeronautical Sciences
September 6-10, 2021
Pudong Shangri-La, Shanghai, China

NUMERICAL INVESTIGATION ON FLOW INTERFERENCE BETWEEN BLENDED-WING-BODY AIRCRAFT AND OVERHANGING NACELLE

Aoxiang Qiu, Weimin Sang, Run Pang

School of Aeronautics, Northwestern Polytechnical University

Abstract

By means of numerically solving three-dimensional Reynolds-averaged Navier-Stokes equations using the Spalart-Allmaras turbulence model, the investigation completed the simulations of the flow interference between blended-wing-body aircraft and overhanging nacelles in taking-off and climbing process. Three model configurations, included the clean airframe, the clean airframe with the V-tails and the clean airframe with the V-tails and powered nacelles, were studied comparatively for analyzing powered nacelles installation effects. Further, the variations of pressure distribution and intake distortion were investigated when the engine fan power and longitudinal positions changed. It seemed that the intake flow of powered overhanging nacelles aggravates the development of flow separation, and the exhaust flow reduces the pressure on the V-tails' inner surface, especially the area around the leading edge. The engine inlet velocity and the longitudinal position of nacelles were selected optimally, in order to maintain lift force and reduce intake distortion.

Keywords: Blended-wing-body configuration. Taking-off and climbing process. Aerodynamic characteristics. Overhanging nacelles. Intake distortion.

1. General Introduction

Placed great expectations to meet the goal of reducing noise, emissions, and fuel burn, the Blended-Wing-Body (BWB) configuration has been regarded as a hot spot in the development of Green Aviation. In this research field, the installation of the engine nacelle mounted on BWB aircraft is a critical issue unsolved. When the aircraft is in the process of take-off and climb, usually at the typical flight conditions of low speed and high angle of attack, there is significant flow interference between the airframe and overhanging nacelles. In recent ten years, researchers have made efforts to demonstrate the problem in experimental and computational ways.

In 2012, Gregory et al [1] interpreted that the addition of the flow through nacelles produces a slight additional increment in nose-down pitching moment, and variation in longitudinal position of flow through nacelles and vertical tails showed little effect on lateral/directional stability in the experimental investigation. Besides, Concerns were raised about vortical flows forming on the forebody and impacting the engine inlets and/or the vertical tails. Subsequently, in 2014, Dan et al [2] explored the use of particle image velocimetry (PIV) measurements to characterize the upper-surface aft-body aerodynamics near the nacelle inlet at various angle-of-attack and sideslip values. None of the experimental investigations showed a vortex propagating through the nacelle but the close proximity was enough to cause concern considering these were flow through nacelles without any engine induced mass flow. Afterwards, in 2016, Melissa and Daniel et al [3-4] completed the experimental and computational evaluation of Inlet distortion on an ejector powered hybrid wing body at take-off and landing conditions. They found a small vortex being ingested during spool up although distortion levels remained within acceptable limits. In the same year, Patrick et al [5] investigated how the jet exhaust influenced the control surface performance as related to the resultant forces and moments on the model, conducting testing on a 5.75% scale hybrid wing body model using turbine powered simulators. They found that the center elevon and vertical tail control authority increased with the jet exhaust from the turbine powered simulator units, compared to flow-through nacelle testing on the same hybrid wing body model. The ejector powered nacelles is considered to perform better than flow through nacelles to simulate the engine operation, and the turbine powered simulator (TPS) is the most advanced device at present, though costs greatly. The above is mainly about experimental research, and the following is the computational work.

In 2016, Wesley [6] carried out computational studies to assess engine operability for an Ultra High Bypass (UHB) engine installation on a Hybrid Wing Body (HWB) aircraft. They thought, at certain aircraft operating conditions at the boundary of the flight envelope, such as 0.2 flight Mach with very high angle of attack or takeoff with 30 knot crosswinds, the installed engine flow field and inlet distortion may differ from what has been typical for conventional tube-wing aircraft with underwing podded engines. In the same year, Joseph et al [7] performed extensive Computational Fluid Dynamic (CFD) simulations for everything from sting design and placement for both the HWB aircraft and ejector powered nacelle systems to the placement of aero-acoustic arrays to minimize its impact on vehicle aerodynamics. When predicting high angle of attack CFD flow field, they found that, resolved pseudo-turbulence occurred in the non-time-accurate results, which was unphysical. A truly time-accurate solution is supposed to be pursued in the similar research. In 2019, Gu et al [8] and Zhao et al [9] researched on engine layout technology from distinct perspectives. The former focused on the influence of Engine intake and exhaust status on aerodynamic characteristics of aircraft at low and high speed. The latter investigated how the variation of supporting heights and positions of the engine contributes to the change of aerodynamic characteristics. Yu et al [10-11] completed the simulation on powered effects of a BWB aircraft at take-off and cruise condition in 2019 and 2020, without consideration of V-tails. In this investigation, numerical simulation of TPS nacelles would be conducted, also, the powered effects on V-tails would be calculated. The flow separation would be studied in the process of takin off and climbing, with the time-accuracy numerical method.

2. Numerical Approach

2.1 Governing Equations

Although the external flow around the BWB aircraft is incompressible during take-off and climb, the air flow in the engine is usually subsonic, of which the Mach number might be up to 0.5. Throughout all the investigations, the governing equations are three-dimensional Reynolds-averaged Navier-Stokes (RANS) equations for compressible viscous turbulent flow, as shown below.

$$\frac{\partial}{\partial t}\iiint_{\Omega}\vec{Q}d\Omega+\oiint_{\partial\Omega}\vec{F}\cdot\vec{n}dS-\oiint_{\partial\Omega}\vec{G}\cdot\vec{n}dS=0 \tag{1}$$

The equations are presented as conservative integral form, convenient to be solved by the finite volume method (FVM). In the formula (1), $\vec{Q}$ stands for the conservative variables. $\vec{F}$ and $\vec{G}$ are convective fluxes and diffusion fluxes, respectively. $\vec{n}$ represents for the unit outward normal vector of surface elements. The formular (2) demonstrates the implications in detail.

$$Q=\begin{bmatrix}\rho\\ \rho u\\ \rho v\\ \rho w\\ \rho E\end{bmatrix}\qquad F=\begin{bmatrix}\rho u & \rho v & \rho w\\ \rho uu+p & \rho uv & \rho uw\\ \rho vu & \rho vv+p & \rho vw\\ \rho wu & \rho wv & \rho ww+p\\ \rho Hu & \rho Hv & \rho Hw\end{bmatrix}\qquad G=\begin{bmatrix}0 & 0 & 0\\ \tau_{xx} & \tau_{yx} & \tau_{zx}\\ \tau_{xy} & \tau_{yy} & \tau_{zy}\\ \tau_{xz} & \tau_{yz} & \tau_{zz}\\ \phi_x & \phi_y & \phi_z\end{bmatrix} \tag{2}$$

The convective terms are obtained by second-order upwind discretization scheme. Quantities at cell faces are computed using a multidimensional linear reconstruction approach.

$$\bar{\varphi}_f=\frac{1}{N_f}\sum_{n}^{N_f}\bar{\varphi}_n\qquad\nabla\varphi=\frac{1}{V}\sum_{f}\bar{\varphi}_f\cdot\vec{A}_f\qquad\varphi_f=\varphi+\nabla\varphi\cdot\vec{r} \tag{3}$$

φ and $\nabla\varphi$ are the cell-centered value and its gradient in the upstream cell, and $\vec{r}$ is the displacement vector from the upstream cell centroid to the face centroid[12].The expression requires the determination of the gradient $\nabla\varphi$ in each cell. The nodal values $\bar{\varphi}_n$ are constructed from the weighted average of the cell values surrounding the nodes. The scheme reconstructs exact values of a linear function at a node from surrounding cell-centered values on arbitrary unstructured meshes by solving a constrained minimization problem, preserving a second-order spatial accuracy. Besides, the diffusion terms are central- differenced. For transient simulations, the second-order implicit temporal discretization is adopted. It is given by

$$\frac{3\varphi^{n+1}-4\varphi^{n}+\varphi^{n-1}}{2\Delta t}=F\left(\varphi^{n+1}\right)\ldots \quad .(4)$$

This method is to evaluate $F(\varphi)$ at the future time level, which is unconditionally stable with respect to time step size. Therefore, both the spatial and temporal discretization for the governing equations can achieve second-order accuracy theoretically.

2.2 Turbulence Models

Solving the closure problem of RANS equations, Boussinesq proposed Eddy viscosity hypothesis. Reynolds stress and mean flow field were connected by eddy viscosity, as shown below.

$$-\rho\left\langle u_i u_j\right\rangle=2\mu_t S_{ij}-\frac{2}{3}\rho k\delta_{ij}k-\varepsilon \quad (5)$$

μ_t is the eddy viscosity (also called turbulent viscosity) coefficient. k is the mean turbulent kinetic energy, and S_{ij} is the mean strain rate. The turbulence models involved in this paper are based on Boussinesq hypothesis, constructing transport equations to compute the eddy viscosity coefficient.

The Spalart-Allmaras (S-A) turbulence model [13] has become popular in recent years, because it has strong robustness to calculate complex flow. Compared with B-L turbulence model, the eddy viscosity field of S-A turbulence model is continuous. Compared with the $k-\varepsilon$ model, S-A turbulence model takes less memory, and has better robustness for external flow problem.

The S-A turbulence model is based on the modified turbulent viscosity $\tilde{v}$ transport equation, which shows the convection term, diffusion term and source term.

$$\frac{\partial\tilde{v}}{\partial t}+u_i\frac{\partial\tilde{v}}{\partial x_i}=c_{b1}\cdot\tilde{S}\cdot\tilde{v}+\frac{1}{\sigma}\left\{\nabla\left[(v+\tilde{v})\cdot\nabla\tilde{v}\right]+c_{b2}\left(\nabla\tilde{v}\right)^2\right\}-c_{w1}f_w\left(\frac{\tilde{v}}{d}\right)^2 \quad (6)$$

$\tilde{S}$ is the modified mean strain rate. d is the minimum distance to the wall. f_w is the source term coefficient. Then, the turbulent viscosity can be calculated in the formula (7). v is the molecular viscosity coefficient. v_t is the turbulent viscosity coefficient.

$$v_t=\tilde{v}f_{v1}\qquad f_{v1}=\frac{\chi^3}{\chi^3+c_{v1}}\qquad \chi=\frac{\tilde{v}}{v} \quad (7)$$

The shear stress transport (SST) turbulence model [14] is a two-equation eddy-viscosity model. The shear stress transport formulation combines the advantage of $k-\omega$ model and $k-\varepsilon$ model. The use of a $k-\omega$ formulation in the inner parts of the boundary layer makes the model directly usable all the way down to the wall through the viscous sub-layer, hence the SST model can be used as a Low-Re turbulence model without any extra damping functions. The SST formulation also switches to a $k-\varepsilon$ behavior in the free-stream and thereby avoids the common $k-\omega$ problem that the model is too sensitive to the inlet free-stream turbulence properties.

The transport equations for the turbulent kinetic energy and the specific dissipation rate are given by

$$\frac{\partial k}{\partial t}+u_i\frac{\partial k}{\partial x_i}=\mu_t S^2-\beta^* k\omega+\frac{\partial}{\partial x_j}\left(\left(v+\frac{v_t}{\sigma_k}\right)\frac{\partial k}{\partial x_j}\right) \quad (8)$$

$$\frac{\partial\omega}{\partial t}+u_i\frac{\partial\omega}{\partial x_i}=\alpha S^2-\beta\omega^2+\frac{\partial}{\partial x_j}\left(\left(v+\frac{v_t}{\sigma_\omega}\right)\frac{\partial\omega}{\partial x_j}\right)+2\left(1-F_1\right)\frac{\sigma_{\omega2}}{\omega}\frac{\partial k}{\partial x_j}\frac{\partial\omega}{\partial x_j} \quad (9)$$

Within the SST turbulence method, the turbulence viscosity coefficient is obtained from the expression shown below. a_1 is the low Reynolds number correction factor. F_2 is the switching function.

$$v_t=min\left(\frac{a_1 k}{\Omega F_2},\frac{k}{\omega}\right) \quad (10)$$

2.3 Boundary Conditions

Reasonable setting of boundary conditions is essential for solving partial differential equations. In

these numerical simulations, the boundary conditions of non-slip wall and pressure far-field based on Riemannian invariants are selected. Especially, the engine inlet and outlet boundary conditions deserve to be mentioned. When calculating the intake and exhaust flow field characteristics of the engine, the inlet is set as the boundary condition of the pressure outlet, and the nozzle is set as the boundary condition of the pressure inlet. Once, the mass flow rate, bypass ratio, total temperature ratio and total pressure ratio are given, other physical quantities of engine inlet and outlet can be obtained from the Isentropic expressions.

In actual working state of engines, there are high-speed rotating fan blades at the inlet, and the boundary conditions are very complex. In this paper, the intake fan of the engine is calculated approximately as a plane, given the mass flow rate, pressure or inlet velocity. Taking a given mass flow rate as an example, the derivation is as follows.

On the inlet plane, the mass flow is defined as follows：

$$\dot{m} = \rho_{fan} q_{fan} A_{fan} = \rho_{\infty} q_{\infty} A_{\infty} \tag{11}$$

And the mass flow ratio is defined as follows:

$$MFR = \frac{A_{\infty}}{A_{HL}} = \frac{\rho_{fan}}{\rho_{\infty}} \frac{q_{fan}}{q_{\infty}} \frac{A_{fan}}{A_{HL}} \tag{12}$$

The positions of A_{∞}, A_{HL} and A_{fan} are illustrated in Figure 1. A_{HL} is determined by the location of the stagnation point, separating the internal and external flow of engines.

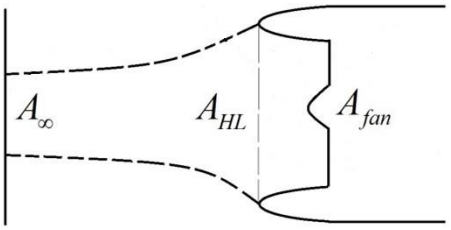

Figure 1 – Longitudinal section of engine air inlet

The definition formula of mass flow ratio is written in the form of formula (13), and the isentropic derivation (14) is substituted,

$$MFR = \frac{A_{fan}}{A_{HL}} \frac{\rho_{fan}}{\rho_{0\infty}} \left(M_{fan} \frac{a_{fan}}{a_{0\infty}} \right) \frac{\rho_{0\infty}}{\rho_{\infty}} \frac{a_{0\infty}}{q_{\infty}} \tag{13}$$

$$\begin{cases} \dfrac{\rho_{fan}}{\rho_{0\infty}} = \left(1 + \dfrac{\gamma - 1}{2} M_{fan}^2 \right)^{-\frac{1}{\gamma - 1}} \\ \dfrac{a_{fan}}{a_{0\infty}} = \left(1 + \dfrac{\gamma - 1}{2} M_{fan}^2 \right)^{-\frac{1}{2}} \\ \dfrac{\rho_{0\infty}}{\rho_{\infty}} = \left(1 + \dfrac{\gamma - 1}{2} M_{\infty}^2 \right)^{\frac{1}{\gamma - 1}} \\ \dfrac{a_{0\infty}}{q_{\infty}} = \left(\dfrac{\gamma - 1}{2} + \dfrac{1}{M_{\infty}^2} \right)^{\frac{1}{2}} \end{cases} \tag{14}$$

In this way, when the mass flow is given, the Mach number at the fan can be obtained, and then the physical quantities of the fan blade at the inlet can be determined.

The total temperature ratio, total pressure ratio and bypass ratio are given to determine the exhaust boundary conditions of the engine. The total temperature ratio and total pressure ratio can be divided into fan / core, and the bypass ratio is the ratio of the mass air flow through the bypass and the mass air flow through the core engine. The intake air of a real engine is divided into two parts. One is directly discharged by the external duct to form the main thrust, and the other is passing through the core

engine. As for that the fuel is burned in the core engine, the mass of the fuel is relatively a small amount to the air mass, which can be ignored. the exhaust mass flow of the internal and external ducts can be calculated from the intake mass and bypass ratio of the engine.

In order to verify the reliability of the intake and exhaust numerical simulation method mentioned above, the turbine powered simulation (TPS) engine wind tunnel test model of Japan Institute of Aeronautics and Astronautics "NAL-AERO-0201" [15] is selected. The meridian plane section shape is shown in Figure 2, and the overall model rotates 360 degrees around the central axis from the meridian plane. This is a typical turbofan engine, with separate exhaust passing through internal and external ducts, which is mostly used in civil and military transport aircraft.

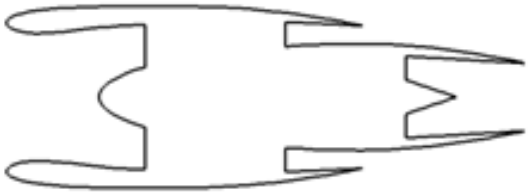

Figure 2 – Meridional plane of the TPS engine

Taking the maximum diameter of the engine model as the reference length, the Reynolds number of the calculated state is 1 million, the angle of attack is 0 degrees, and the Mach number is 0.5/0.6. The parameters of the two intake and exhaust states are shown in Table 1.

Table 1 – Intake and exhaust status parameters

M_∞	MFR	$P_{0F}/P_{0\infty}$	$T_{0F}/T_{0\infty}$	$P_{0C}/P_{0\infty}$	$T_{0C}/T_{0\infty}$
0.5	0.699	1.5046	1.1486	0.0652	0.6837
0.6	0.496	1.2057	1.0634	0.1003	0.7480

Figure 3 shows the comparison between the numerical simulation results and the wind tunnel test results of TPS engine surface pressure coefficient distribution. The coordinate X in the figure represents the actual axial dimension. Under the two intake and exhaust conditions of the engine, the calculated values of the pressure coefficient distribution on the surface of the nacelle inlet, cover and inner wall are in good agreement with the experimental values, which can verify the reliability of the intake and exhaust boundary condition mentioned above.

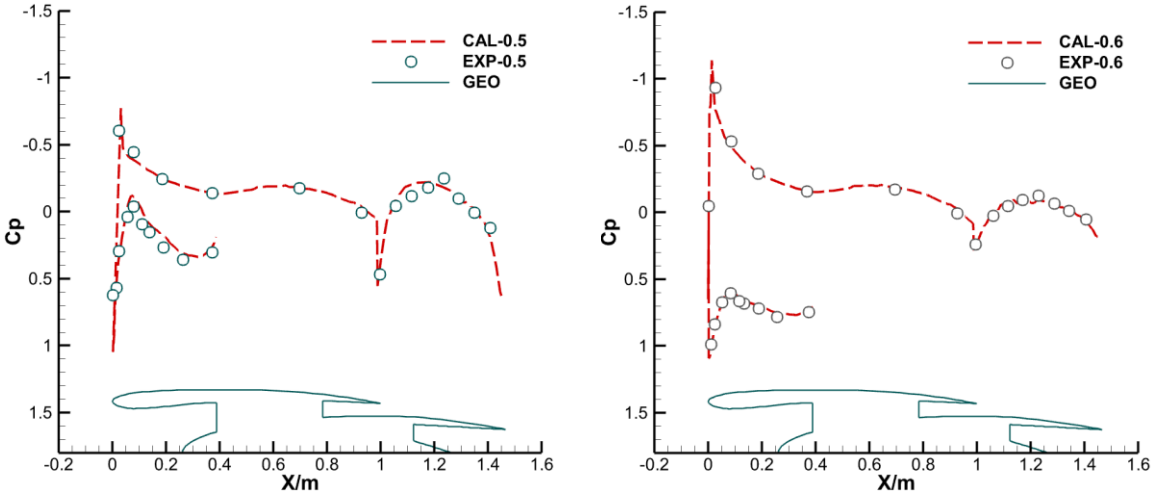

(a) M_∞=0.5 (b) M_∞=0.6

Figure 3 – Comparison of surface pressure coefficient distribution between computational & experimental results of TPS engine

3. Method Validation

3.1 Grid Convergence Study

In this section, the BWB aircraft N2A (a clean airframe) was selected for grid convergence study. A series of Multi-block structured grids for N2A was generated. Grid topology is sketched in Figure 4.The

number of grid cells ranges from 6 million to 54 million. Even the sparest grid can attain the goal that the first grid height off the wall leads y^+ <1. The Reynolds number of this calculated state is 6.6 million, the angle of attack is 15 degrees, and the Mach number is 0.2, identical to take-off flight conditions.

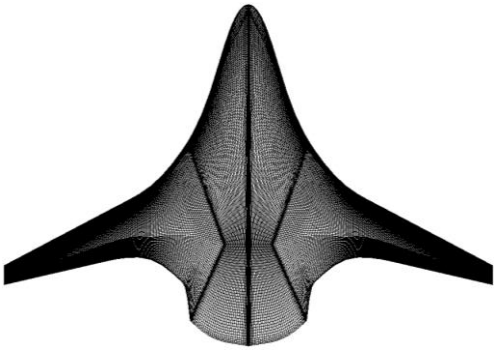

Figure 4 – Surface grid topology for N2A

Table 2 shows that the error level of lift coefficient varies with the grid numbers. Figure 5 reveals that the S-A and SST turbulence model have different convergence characteristics for the grid. When the number of grid isn't so adequate, SST performs better than S-A. With the grid becoming finer and finer, the advantage of convergence characteristics is apparent with respect to the S-A turbulence model. The dotted lines represent the extrapolation for an infinite grid, and the black hollow point marks the experimental value $C_l\big|_{\alpha=15^\circ} = 0.643$ [1].

Table 2 – Error of the calculated lift coefficients

(Grid/Million)	G_1=6	G_2=12	G_3=18	G_4=28	G_5=40	G_6=54	G_∞
S-A	-8.71%	-6.84%	-5.75%	-4.98%	-4.35%	-3.89%	-1.71%
SST	-8.24%	-7.00%	-6.38%	-6.28%	-5.60%	-5.28%	-4.04%

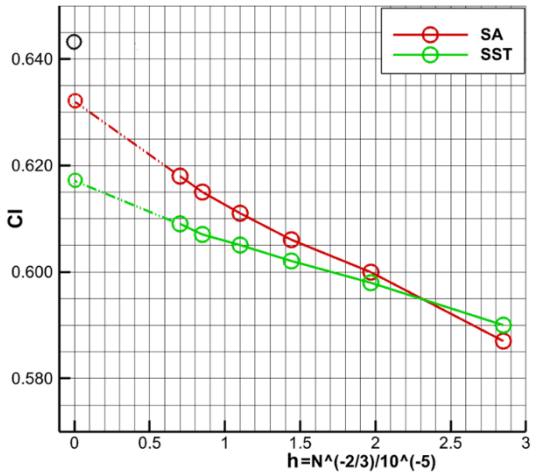

Figure 5 – Convergence characteristics of S-A and SST

Consequently, in the following research, the S-A turbulence model is preferred. As for the scale of grids, the scale same as that of the grid G_4 ought to be selected, which is full in consideration of the accuracy of results and the efficiency of calculations.

3.2 Example Case Verifaction

In order to validate the numerical method for solving the external flow field of aircrafts, on the basis of the calculation in section 3.1, the cases of clean N2A airframe, whose attack angles ranges from -10 to 20 degrees, were simulated using the grid G_4 and S-A turbulence model. Comparing the calculated force coefficients with experimental data, we could find that they reached a good agreement.

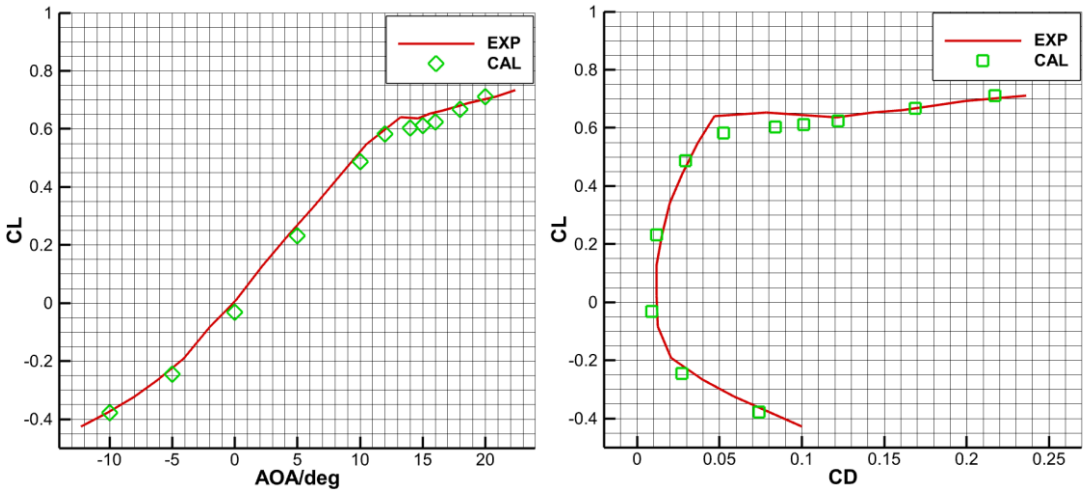

(a) CL-AOA (b) CL-CD

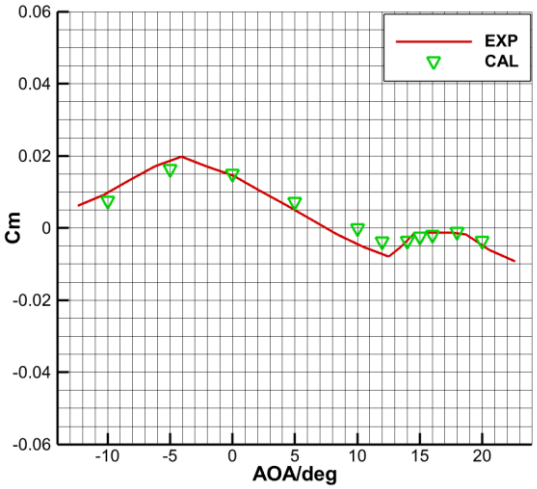

(c) Cm-AOA

Figure 6 – Force coefficients comparisons

What's more, it can be seen from Figure 7 that, the flow separation begins when the attack angle is 12 degree, and the streamline form tends to be stable after the attack angle is 18 degree, which is identical to the change of the lift curve slope. Next, the investigation would focus on the complex flow when the attack angles range from 12 to 18 degree.

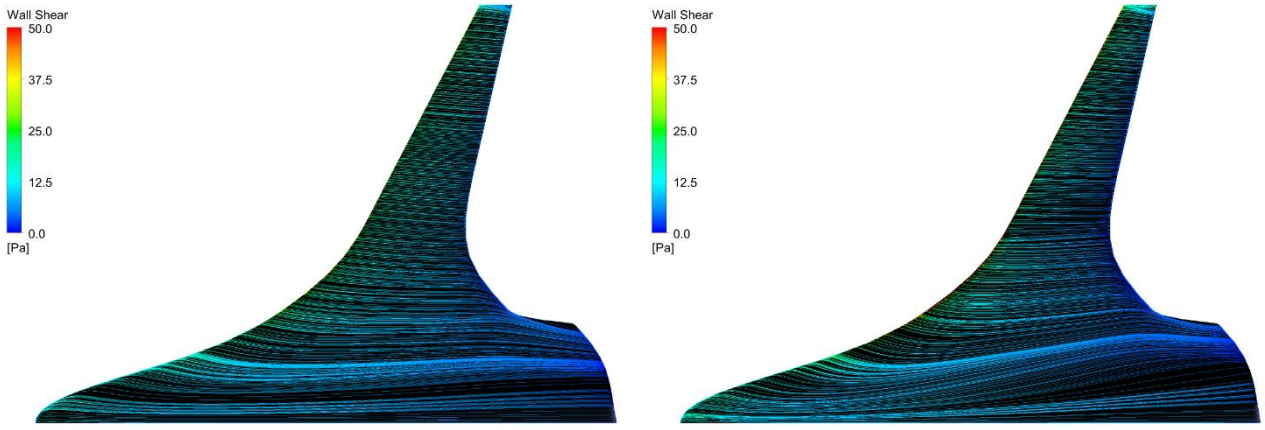

(a) AOA=5° (b) AOA=10°

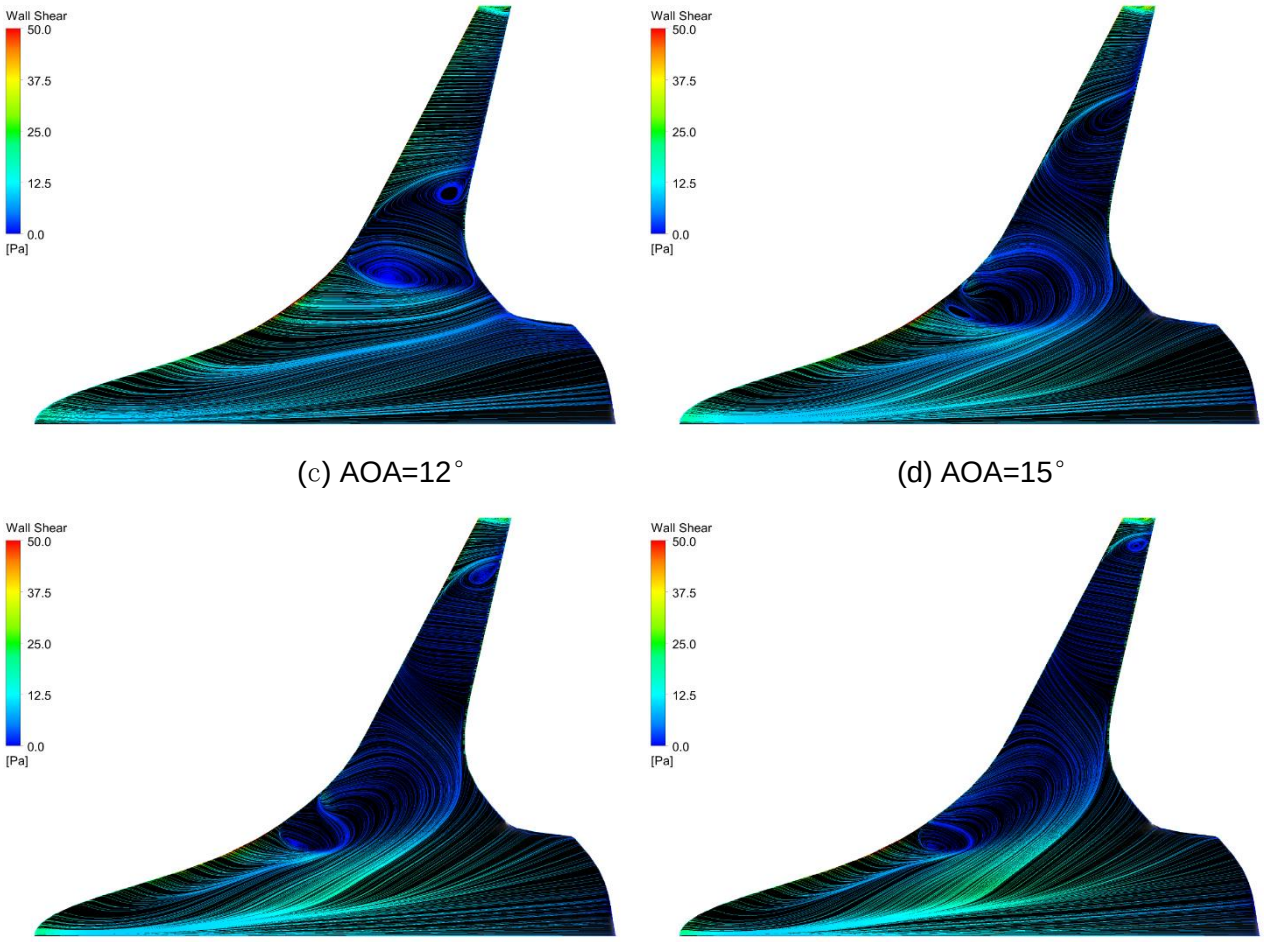

(c) AOA=12°　　(d) AOA=15°

(e) AOA=18°　　(f) AOA=20°

Figure 7 – Surface streamlines combined with wall shear contours

4. Results and Analysis

In the following sections, three model configurations, included the clean airframe, the clean airframe with the V-tails and the clean airframe with the V-tails and powered nacelles, were studied comparatively. The clean airframe is N2A model shown in section 3.1, and the others are shown below. The cross-section of the V-tails is NACA 0006 airfoil, and the V-tails were set with 10 degree cant angle outwards. The nacelles were selected from DPW-Ⅱ, with 30% lager diameters.

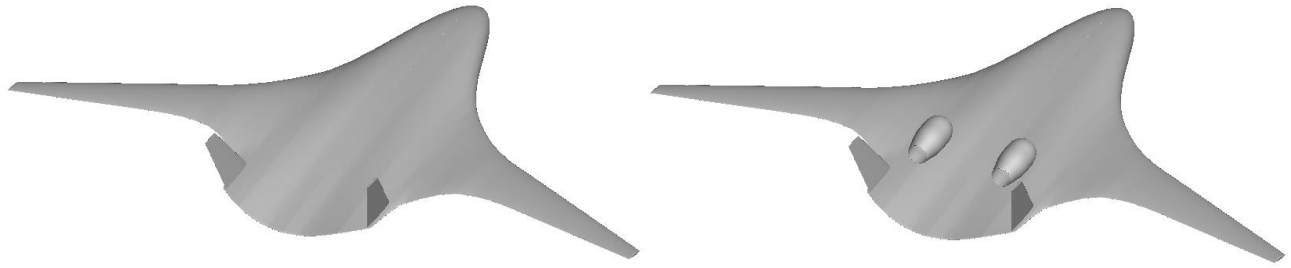

(a) With the V-tails　　(b) With the V-tails and powered nacelles

Figure 8 – Model configurations

4.1 Powered Nacelles Installation Effects

In this section, V-tails and nacelles installation effects were calculated and analyzed from the cases of three model configurations when the attack angle is 12, 15, and 18 degrees. The Reynolds number and Mach number were the same as those in section 3.1, which maintains the flight conditions of low speed and high attack angles. By the way, the physical condition and longitudinal position of the powered nacelles will be shown as the baseline speed condition and position in section 4.2 & 4.3.

Figure 9 shows the comparations of pressure coefficients and skin frication coefficients on the upper surfaces of the three model configurations. The left halves imply that the intake flow affects the

pressure distribution of the wing body joint. Skin frication coefficients can mark the flow separation part on the surface, since that of separated flow region is significantly lower than that of attached flow region Observing with the right halves, the intake flow aggravates the development of flow separation. For example, when the attack angle is 15 degrees, the flow separation ends in the middle of the wing without the powered nacelles. However, with the powered nacelles, the flow separation extends to the wing tip nearly.

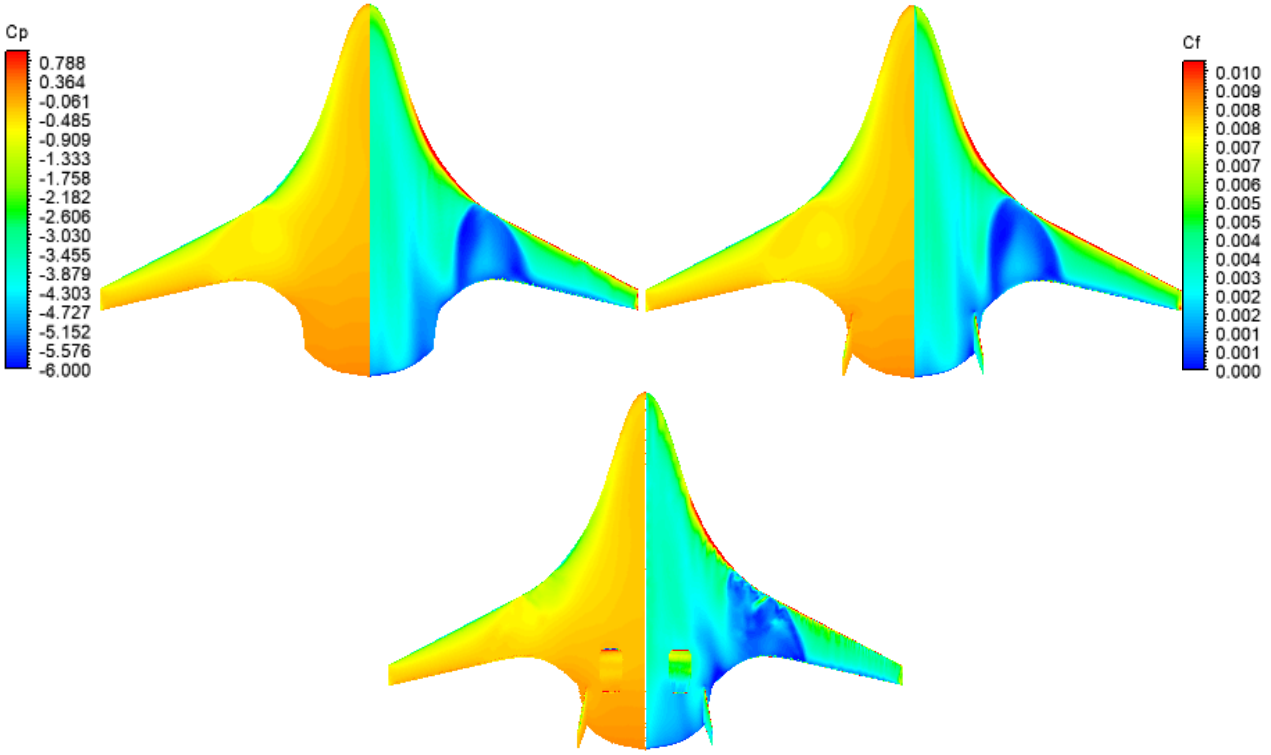

(a) AOA=12°

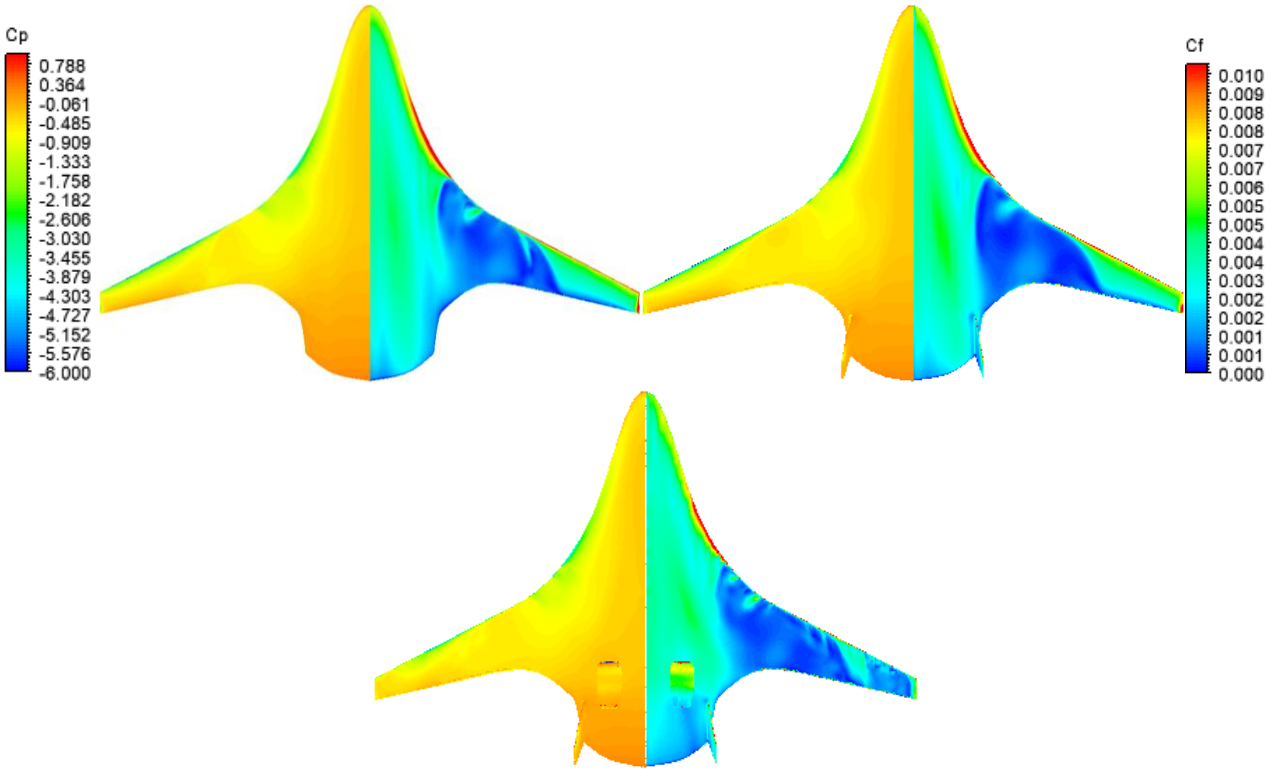

(b) AOA=15°

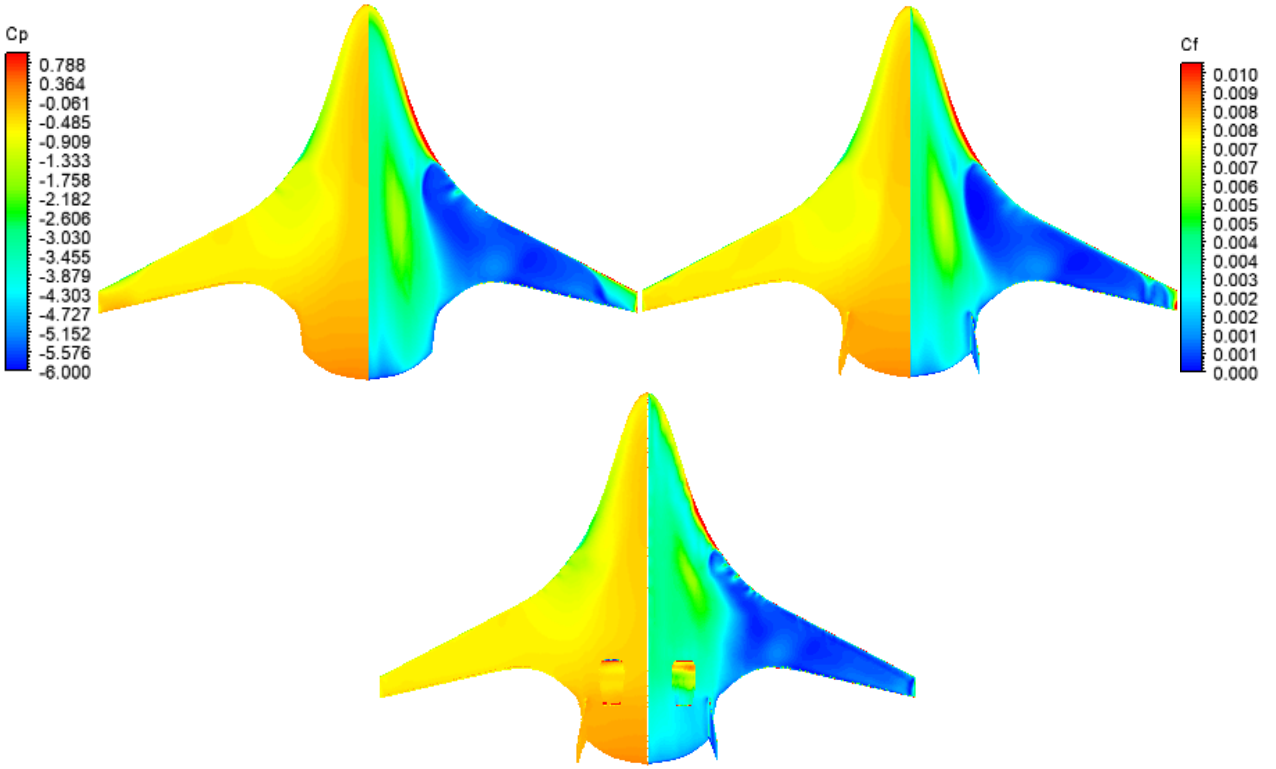

(c) AOA=18°

Figure 9 – Comparations of surface pressure and skin frication

Figure 10 shows the comparations of surface pressure on V-tails between the two configurations. It can be seen that the exhaust flow reduces the pressure on the inner surface, especially around the leading edge. With the increase of attack angles, the boundary of influence area gradually develops to the middle. The exhaust flow shows little effects on the outer surface. Only when the attack angle is 18 degrees, the bottom of the leading edge of the outer surface appears an apparent low pressure region, which seems to be induced by the flow separation. From Figure 9 (c), the separated flow occurs around the V-tails, and the separation without the powered nacelles is slight.

(1) With the V-tails (2) With the V-tails and powered nacelles

(a) AOA=12°

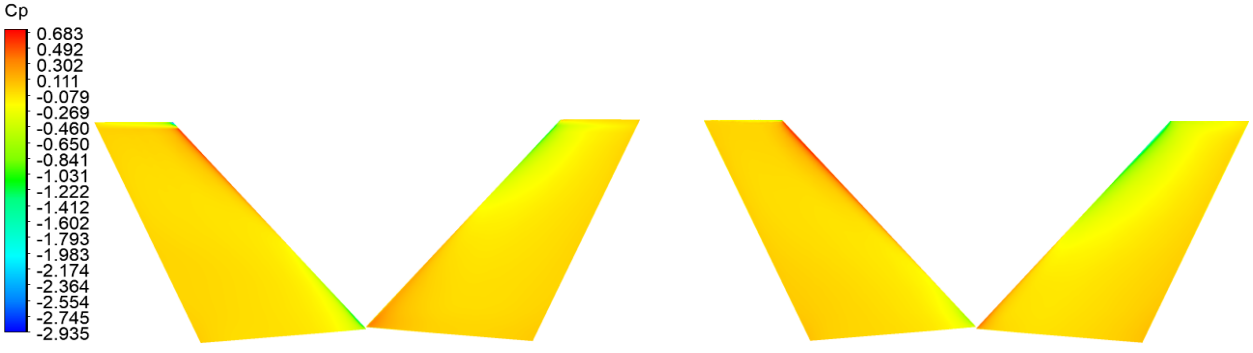

(1) With the V-tails (2) With the V-tails and powered nacelles

(b) AOA=15°

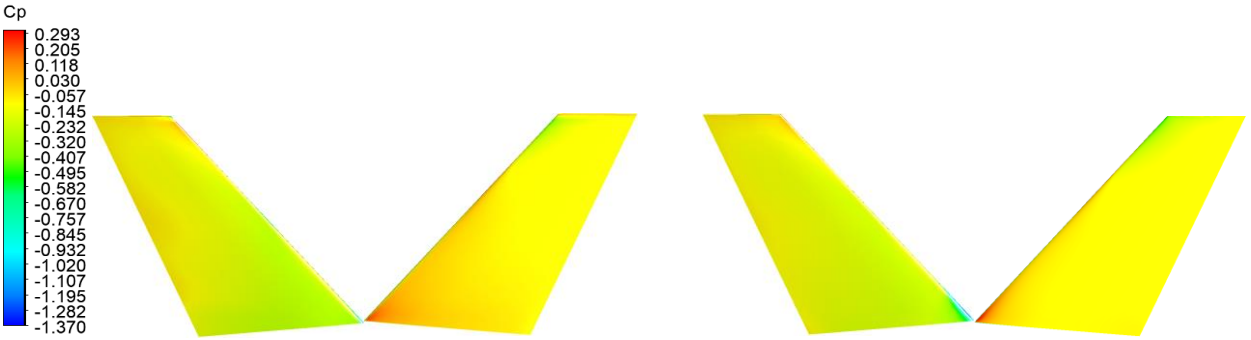

(1) With the V-tails (2) With the V-tails and powered nacelles

(c) AOA=18°

Figure 10 – Comparations of surface pressure on V-tails

4.2 Engine Inlet Velocity Variations

In this section, the engine inlet velocity was changed. Regarded the engine condition used in section 4.1 as a baseline condition, we calculated the flow field when the inlet velocity increased and decreased. The detailed inlet and outlet boundary conditions are shown below. With the inlet velocity variating, there are corresponding changes of the mass flow through the nacelles. In order to keep the mass flow balance, the total pressure and total temperature were also changed.

Table 3 – Intake and exhaust status parameters

	M_{FAN}	P_{FAN}/P_{∞}	$T_{0N}/T_{0\infty}$	$P_{0N}/P_{0\infty}$
HIGH	0.50	0.8669	0.7896	1.1098
BASIC	0.45	0.8949	0.8024	1.0916
LOW	0.40	0.9209	0.8199	1.0628

Figure 11 shows that the comparations of Mach number contours under the three engine conditions. It is clearly embodied in the picture that the inlet and outlet velocity variations have rational change tendency. Although it only shows the velocity field of 18 degrees of attack angle, those of 12 and 15 degrees of attack angles can illustrate the same conclusion.

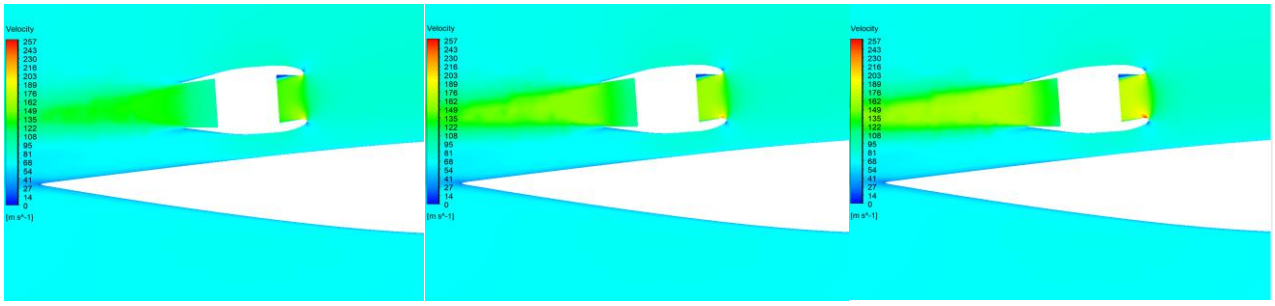

(a)LOW (b) BASIC (c) HIGH

Figure 11 – Mach number contrast when the engine inlet velocity variates

The pressure distributions on three feature sections were investigated. Figure 12 shows the positions of these sections. All locates around the wing body joint area, which is considered to be of major impact, concluded from the section 4.1. In the figure, η is the fractional of the semi-span.

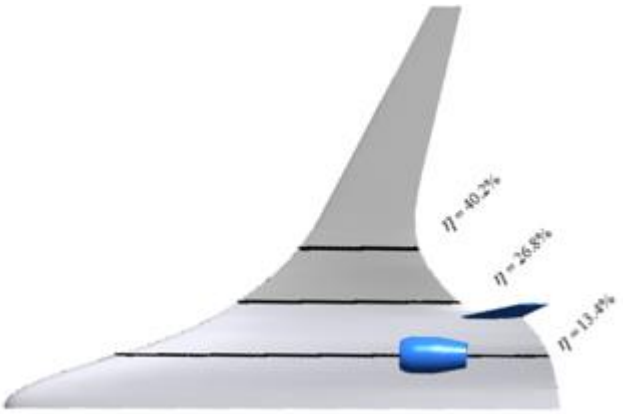

Figure 12 – Positions of three feature sections

Figure 13 shows the comparations of pressure coefficients under different engine conditions. From these sketches, it can be found that the effect of the intake and exhaust flow gradually decreases when the angle of attack increases. For the section η=13.4%, the high engine inlet velocity brings low surface pressure, especially on the longitudinal position ranging from x/c=0.4 to x/c=0.6 (the lip section locates at x/c=0.72). there is the slightest impact on the section η=26.8%. With respect to the section η=40.2%, where happens the core flow separations, the pressure of the leading edge is sensitive to the variations of the engine inlet velocity. From the view of maintaining the lift, the basic engine inlet velocity in the investigation is of underperformance. Upper or lower inlet velocity will be preferred.

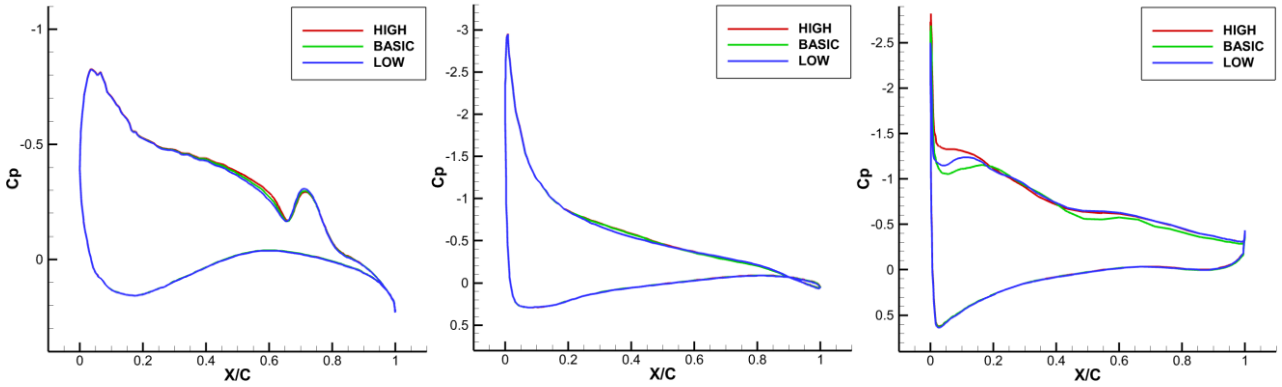

(1) η=13.4% (2) η=26.8% (3) η=40.2%

(a) AOA=12°

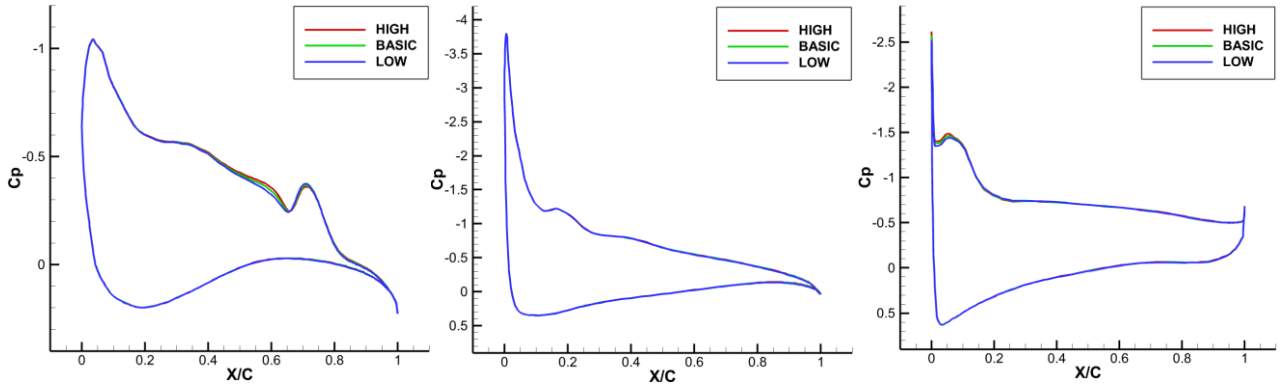

(1) η=13.4% (2) η=26.8% (3) η=40.2%

(b) AOA=15°

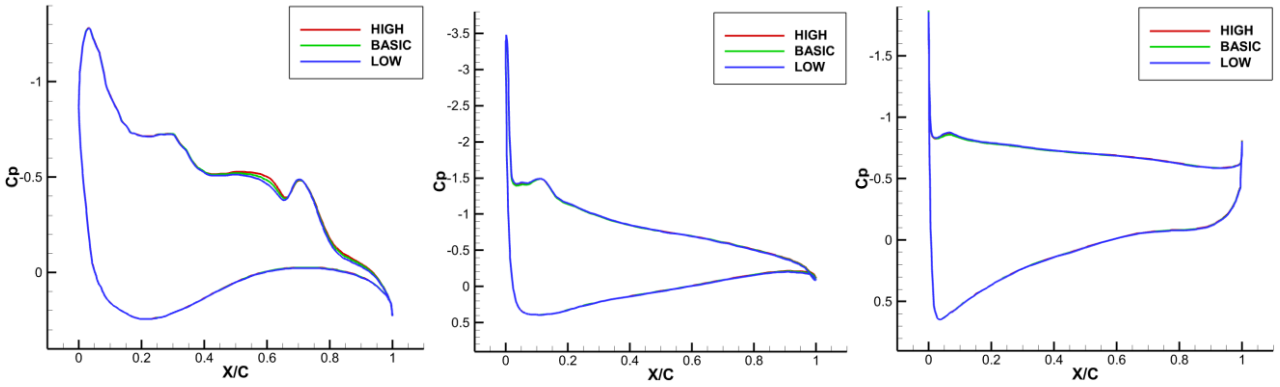

(1) η=13.4% (2) η=26.8% (3) η=40.2%

(c) AOA=18°

Figure 13 – Comparations of pressure coefficients under different engine conditions

4.3 Longitudinal Positions of Nacelles

In this section, three longitudinal positions of nacelles, shown in the table 4, were set for the investigation on the problem of intake distortion. X_{tip} represents the longitudinal of the tip, and L is the length of the aircraft. Usually, the intake distortion contains the total pressure distortion and the total temperature distortion. Under the current flow conditions, the total temperature distortion isn't significant. The following results just focus on the total pressure distortion.

Table 4 – Longitudinal positions of nacelles

	Forward	Baseline	Backward
X_{tip}/L	0.64	0.72	0.80

Figure 14 shows the comparations of total pressure on the engine inlet. The inlet section was selected from the engine on the right side, and it was considered to be symmetric. The circumferential influence range indicates the intensity of intake distortion. From the view of reducing distortion, the backward position among the investigation is supposed to be chosen. Although, the position influence seems to affect rarely when the angle of attack is 12 and 15 degrees. With the angle of attack increasing, the advantage of the backward position is gradually obvious.

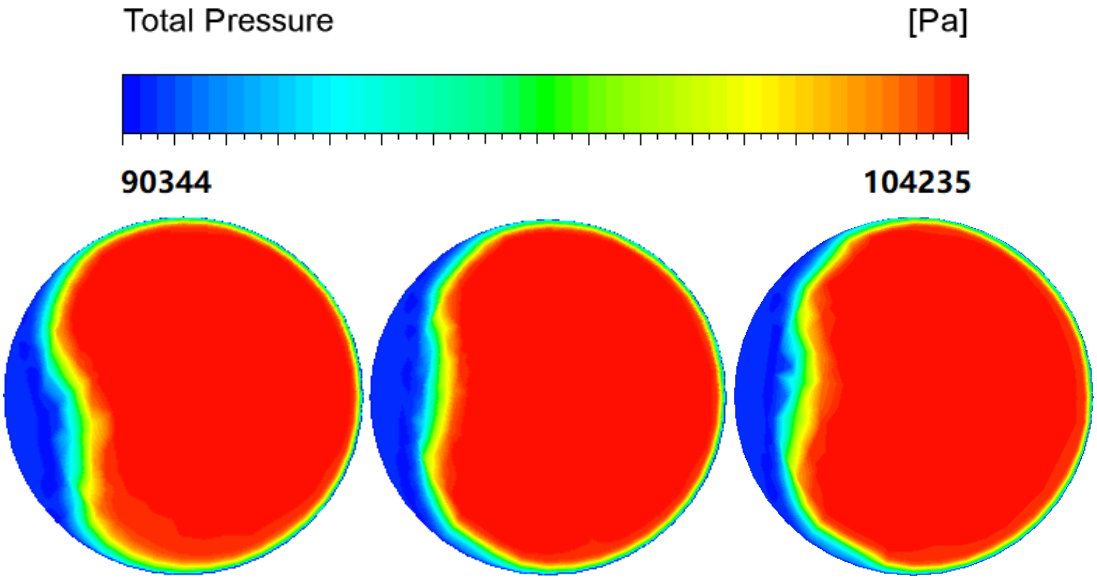

Forward Baseline Backward

(a) AOA=12°

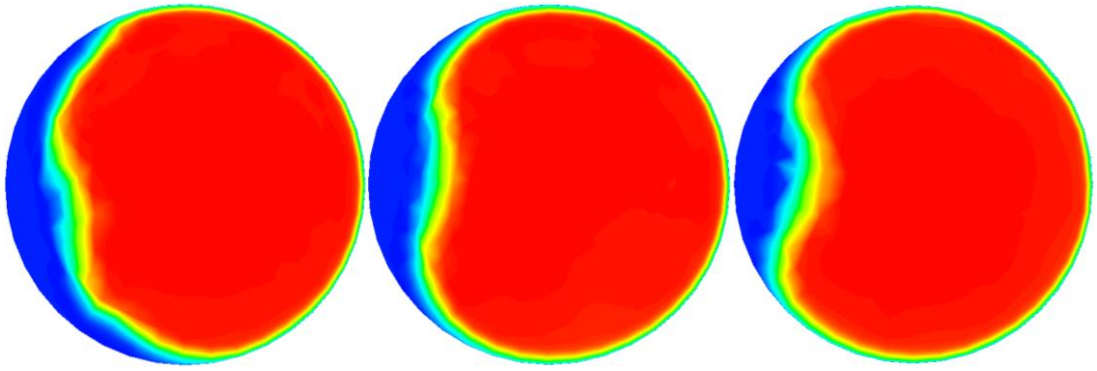

Forward Baseline Backward

(b) AOA=15°

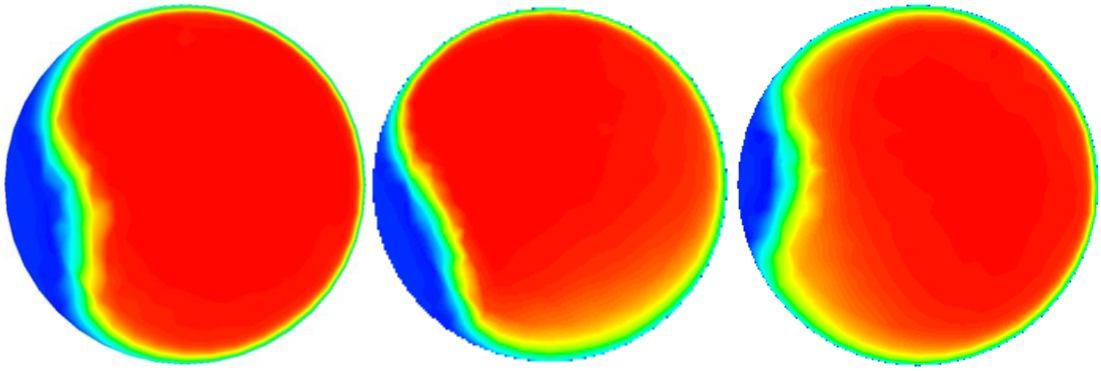

Forward Baseline Backward

(c) AOA=18°

Figure 14 – Comparations of total pressure on the engine inlet

5. Conclusions

Having completed the numerical investigations on the flow interference between BWB aircrafts and overhanging nacelles, we come to the following conclusion:

a. In the process of taking off and climbing, the flow interference of the engine impacting on the aircraft turns out to be that the intake flow of powered overhanging nacelles aggravates the development of flow separation, and the exhaust flow reduces the pressure on the V-tails' inner surface, especially the area around the leading edge.

b. In the purpose of maintaining the lift force, the basic engine inlet velocity in the investigation is of underperformance. Upper or lower inlet velocity will be preferred.

c. The flow interference of the BWB aircrafts impacting on the engine is incarnated in the intake distortion. From the view of reducing distortion, the backward position is supposed to be chosen.

6. Acknowledgement

This work has benefited greatly from the support of the Aeronautic Science Foundation of China under grant 2018ZA53014 and the Open Fund of Key Laboratory of Icing and Anti/De-icing of China under grant IADL20200101.

7. Contact Author Email Address

For facilitating future contacts. please mail to: sangweimin@nwpu.edu.com.

8. Copyright Statement

References

[1] Gregory G, Dan D, Vicroy D, et al. experimental investigation of the low-speed aerodynamic characteristics of a 5.8-percent scale hybrid wing body configuration. *30th AIAA Applied Aerodynamics Conference*, New Orleans, Louisiana, 2012.

[2] Vicroy D, Gregory M, Jenkins N, et al. Low-speed aerodynamic investigations of a hybrid wing body configuration. *32nd AIAA Applied Aerodynamics Conference*, Atlanta, Georgia, 2014.

[3] Melissa B, Shea R, Flamm D, et al. Experimental evaluation of Inlet distortion on an ejector powered hybrid wing body at take-off and landing conditions. *54th AIAA Aerospace Sciences Meeting*, San Diego, California, 2016.

[4] Daniel T, Tompkins D, Deere K A, et al. computational evaluation of inlet distortion on an ejector powered hybrid wing body at takeoff and landing conditions. *54th AIAA Aerospace Sciences Meeting*, San Diego, California, 2016.

[5] Patrick R, Flamm D, Long K, et al. Turbine powered simulator calibration and testing for hybrid wing body powered airframe integration. *54th AIAA Aerospace Sciences Meeting*, San Diego, California, 2016:

[6] Wesley K. Lord, Gavin J. Hendricks, and Michael J. Kirby. Impact of ultra high bypass/hybrid wing body integration on propulsion system performance and operability. 54th AIAA Aerospace Sciences Meeting, San Diego, California, 2016:

[7] Joseph A, Melton J, Schuh J, et al. NASA ERA integrated CFD for wind tunnel testing of hybrid wing-body configuration. 54th AIAA Aerospace Sciences Meeting, San Diego, California, 2016:

[8] Gu WT, Chen YC, Xin ZQ, et al. Intake and exhaust effect on aerodynamic characteristics of blended wing body civil aircraft with podded engines. *Journal of Aerospace Power*, Vol. 34, No. 6, pp 1297-1310, 2019 (in Chinese).

[9] Zhao ZS, Feng J, Miao SM, et al. Research on blended-wing-body aircraft overhanging engine layout technology based on numerical simulation. *Acta Aeronautica et Astronautica Sinica*, Vol. 40, No. 9, 2019 (in Chinese).

[10] Yu G, Li D, Shu Y, et al. Numerical simulation for engine/airframe interaction effects of the BWB300 on aerodynamic performances. *International Journal of Aerospace Engineering*, Vol. 2019, 2019.

[11] Yu G; Li D and Zhang ZY. Simulation on powered effects of BWB at take-off condition. *Journal of Northwestern Polytechnical University*, Vol. 38, No. 2, pp 231-237, 2020 (in Chinese).

[12] Barth T and Jespersen D. The design and application of upwind schemes on unstructured meshes. *27th Aerospace sciences meeting*, Reno, Nevada,1989.

[13] Menter R. Two-equation eddy-viscosity turbulence models for engineering applications. *AIAA Journal*, Vol. 32, No. 8, pp 1598-1605, 1994.

[14] Spalart R and Allmaras R. A one-equation turbulence model for aerodynamic flows. *30th Aerospace Sciences Meeting and Exhibit,* Reno, Nevada, 1992.

[15] Naoki K, Kisuke A, Katsuya I. Transonic 3-D Euler analysis of flows around fanjet engine and TPS.(Turbine Powered Simulator). NAL-TR-1045, 1989 (in Japanese).